Fast Prediction of 2D Airfoil Flows Based on the U-Net Framework with Multi-Strategy Evaluation

Junqiao Wang*,Chen Liu*,Xinyu Zhang*
Corresponding author: Chen Liu
* Harbin Engineering University, China.

Abstract: This study investigates fast prediction of two-dimensional airfoil flow fields using a U-Net-based framework with attention mechanisms, physics-informed constraints, and multi-objective optimization. A database of 740 NACA0012 flow cases was generated by RANS simulations over Mach numbers of 0.1–0.3, Reynolds numbers of 3.0×10^6–9.0×10^6, and angles of attack from −1° to 8°. The baseline U-Net predicts pressure and velocity fields with good global agreement with RANS results, while larger errors remain near the boundary layer, leading edge, and wake. Comparative evaluations show that generic attention reweighting does not consistently improve prediction accuracy, because learned attention may not align with physically important thin-layer flow structures. Physics-informed soft constraints improve near-wall accuracy and physical consistency, but may increase global regression error because of competition between data-fitting and physical-residual objectives. Multi-objective optimization further reveals gradient conflicts among pressure and velocity targets. In particular, the gradient-conflict-resolution strategy reduces the global and local pressure-field relative errors by 30.0% and 21.7%, respectively, compared with the baseline U-Net. The PIUN model achieves up to a 61.2% reduction in local relative error, although global error can increase. These results highlight the trade-offs among data accuracy, physical consistency, and multi-output optimization in rapid airfoil flow prediction..

Keywords: Computational Fluid Dynamics, Machine Learning, Physics Informed, Airfoil, Flow field prediction.

1. Introduction

Over the past few decades, with the continuous advancement of Computational Fluid Dynamics (CFD)numerical simulation methods have been widely applied in the field of aerodynamics. [1-8] However.as CFD calculations advance toward higher fidelity, the computational time required for iterative solutions also increases dramatically. [9] In recent years, machine learning (ML) has been advancing at an unprecedented pace. It has achieved success in fields such as computer vision [10], natural language processing [11], and autonomous driving [12], and is gradually becoming a research methodology for solving specific problems [13]. Accordingly, the data-processing strengths of machine learning have made Machine Learning for CFD an emerging research focus in fluid mechanics. [14, 15].

As one of the supervised learning methods, deep learning (DL) holds promise to replace costly and time-consuming traditional iterative solutions [16, 17]. Sun et al. [18] proposed a deep neural network-based method for predicting compressible flow over transonic airfoils. Results demonstrate that this approach maintains high resolution and computational efficiency while exhibiting strong generalization capabilities, making it suitable for optimizing supercritical airfoil designs. Thuerey et al. [19] constructed a simulation dataset using the Reynolds-Averaged Navier-Stokes (RANS) model in Open-FOAM. They employed a deep U-Net architecture to predict pressure and velocity distributions in incompressible flow fields around airfoils, investigating the impact of dataset size and model weights on prediction accuracy, Furthermore the optimized model achieved mean relative errors below 39 for two unseen airfoil flow field predictions Chen et al. [20] proposed a supervised learning-based method for predicting velocity and pressure fields around arbitrarily shaped obstacles in two-dimensional laminar flow, Results demonstrate that the model exhibits strong geometric generalization capabilities while maintaining good physical consistency. Chen and Nil [21] conducted research on the U-Net deep neural network, addressing the problem of accurately inferring solutions for two-dimensional compressible Reynolds-averaged Navier-Stokes (RANS) flows over airfoils. Notably, compared to traditional CNNs, U-Net achieves effective fusion of local and global features through skip connections between up-sampling and down-sampling layers, thereby enhancing the model's feature extraction capability. The aforementioned research demonstrates the effectiveness of deep learning methods in end-to-end flow field prediction. Despite the outstanding performance of convolutional neural networks in extracting spatial features of flow fields, some scholars have pointed out that data-driven surrogate models still fall under the category of black-box models [22]. Duru et al. [23] proposed a deep learning method for predicting transonic airfoil flow fields based on a CNN neural network framework. Results demonstrate that this approach achieves high accuracy and computational efficiency in predicting high pressure gradients and high Mach numbers. Meanwhile, the author also points out that since the Reynolds number effect itself is not particularly significant for flow fields spanning transonic to supersonic regimes, this method exhibits low sensitivity to Reynolds number variations. Consequently, the model performs Unfavorably in predicting flow fields around low-Reynolds-number airfoils. On one hand, this highlights the dependency of traditional deep learning methods on labeled data; on the othe, it demonstrates that data-driven surrogate models cannot automatically achieve physically consistent prediction results.

Compared with data-driven agent models, since the Physics-informed Neural Network (PINN) can directly incorporate the learned fields into the control equations, the results are considered to have good physical consistency. Dong et al. [24] directly solved partial differential equations (PDEs) using neural networks without relying on labeled data. The results demonstrate that this approach can precisely enforce the periodicity of deep neural network (DNN) solutions and their derivatives [24]. Sun et al. [25] proposed a physical-information-based deep learning proxy model construction method that enables airfoil flow field prediction without relying on CFD labeled data, solely by constraining the N-S equation as the loss function. However, while this approach-which bypasses any labeled data and directly employs PDEs as loss functions-ensures the physical consistency of predictions, it struggles to balance both data dimensionality and computational efficiency [26]. However, the method exhibits low sensitivity to changes in Reynolds number, leading to deficiencies in the physical consistency and robustness of the predicted flow fields. Raissi et al. [27] found that compared to supervised learning with labeled data, PINNs require finding solutions by optimizing PDEs residuals. Due to the highly nonlinear nature of PDEs loss terms and weight competition with boundary condition loss, convergence during gradient descent is significantly slower than in supervised learning. Wang et al. [28] found that higher order derivatives from physical constraints can cause the gradient flow of the loss function to exhibit stiffness issues. Under identical accuracy requirements, physical-constrained models require 1-2 orders of magnitude more training iterations than purely data-driven surrogate models. This is because, lacking guidance from labeled data, PINNs spend excessive time exploring feasible physical spaces, resulting insignificantly lower initial convergence efficiency compared to supervised learning [29]. Therefore, some scholars have proposed a neural network model that integrates data-driven approaches with physical information [30]. Gao et al. [31] proposed a data-driven convolutional neural network-based super resolution method incorporating physical constraint regularization. By explicitly introducing conservation laws and boundary conditions into the training process, this approach enables reconstruction of high resolution flow fields from low-resolution inputs without requiring high-resolution labels. Furthermore, Krishnapriyan et al. [32] systematically pointed out that incorporating PDEs soft regularization models may introduce ill-conditioned problems and make the loss landscape harder to optimize. This can lead to models failing to learn key physical phenomena in slightly more complex problems. At the same time, the research also indicated that this failure likely stems not from insufficient network expressiveness, but rather from optimization difficulties arising from the PINNs configuration.

In fact, model training within the framework of physically informed soft constraints typically comprises multiple components, including data supervision terms, boundary supervision constraints, initial value constraints, and PDEs constraints. Bischof and Kraus [33] point out that these loss terms may exhibit competitive relationships during training and emphasize that correctly handling the combination of multiple losses is crucial for model training. This perspective undoubtedly stems from analyzing PINN soft-constrained training within the framework of multi-objective optimization. Therefore, the deterioration in performance of physically constrained data-driven agent models primarily stems from the inherent competition between the data supervision term and the physical residual term during the deep learning process. It is worth noting that this competition between the data supervision term and the physical residual term is not caused by a single factor [34-39]. Notably, because the optimization landscape is non-convex, achieving a Pareto-optimal balance between data fitting and physical consistency does not guarantee improved accuracy of physics-constrained data-driven surrogates models [40, 41]. Furthermore, convergence of the physical residual does not equate to a simultaneous reduction in fitting error. Moreover, approximate calculations of physical loss may introduce trade-offs between bias and variance, rendering optimization and generalization performance sensitive to algorithmic details [42,43].

In summary, this paper investigates a rapid prediction method for two-dimensional airfoil flow fields based on the U-Net framework. Six neural network models were successively established, and the prediction accuracy of different neural network models was analyzed, First, comparative experiments were conducted between the attention mechanism and physical constraints to explore their respective impacts on model prediction accuracy. Second, the study compares the effects of multi-objective optimization methods, including the Multi-Objective Pareto-Aware Algorithm (MOPA) and the Projected Conflicting Gradient Algorithm (PCGA), on model prediction. This examines how potential competition among different physical quantity regression targets affects model training and prediction performance in the joint prediction task of pressure and velocity fields. Furthermore, this paper establishes a physically constrained PIUN neural network model to investigate the predictive performance of data-driven neural network models under different model frameworks. The aim is to systematically analyze the applicability boundaries and performance characteristics of attention mechanisms, physical constraints, and multi-.objective optimization strategies in the prediction of flow fields over regular-grid airfoils, rather than solely pursuing the optimal performance of a single model.

2. Methodology

2.1. Numerical simulation

This paper conducts numerical simulations of two-dimensional airfoil flow fields under various Reynolds number, Mach number, and angle of attack conditions, thereby establishing a two-dimensional airfoil flow field database.

To ensure computational stability and the reliability of simulation results, this study employs the RANS solver in ANSYS Fluent to perform numerical simulations of two-dimensional airfoil flow fields using structured meshes. The governing equations for the airfoil flow field under different flow conditions areas follows:

$$\frac{\partial \rho}{\partial t}+\frac{\partial u_i}{\partial x_i}=0 \tag{1}$$

$$\rho\left(\frac{\partial u_i}{\partial t}+\frac{\partial u_i u_j}{\partial x_j}\right)=--\frac{\partial p}{\partial x_i}+\frac{\partial}{\partial x_i}\left(\mu\left(\frac{\partial \mu_i}{\partial x_j}+\frac{\partial u_j}{\partial x_i}-\frac{2}{3}\delta_{ij}\frac{\partial u_l}{\partial x_l}\right)\right)+\frac{\partial}{\partial x_j}\left(-\rho\overline{u_i' u_j'}\right) \tag{2}$$

$$\frac{\partial \rho u_j}{\partial x_j}=-\frac{\partial p u_j}{\partial x_j}+\frac{\partial}{\partial x_j}\left[c_p\cdot\left(\frac{\mu}{\mathrm{Pr}}+\frac{\mu_t}{\mathrm{Pr}_t}\right)\cdot\frac{\partial T}{\partial x_j}\right]+\frac{\partial}{\partial x_j}\left[u_i\cdot(\mu+\mu_t)\cdot\left(2S_{ij}-\frac{2}{3}\delta_{ij}S_{kk}\right)\right] \tag{3}$$

where x_j denotes the spatial coordinate (j = 1, 2, 3 corresponding to x , y , and z), u , is the velocity component, t denotes time, ρ is the density, and T is the temperature. where u , p , and T represent velocity, pressure, and temperature, respectively, Additionally, S_{ij} denotes the strain-rate tensor,

$$S_{ij} = \frac{1}{2}\left(\frac{\partial u_i}{\partial u_j} + \frac{\partial u_j}{\partial u_i}\right) \tag{4}$$

Where μ and μ_t , represent molecular viscosity and turbulent viscosity, respectively, with the turbulent viscosity determined by the following turbulence model.

Literature indicates that compared to six turbulence models including the RNG k-epsilon model, the SST k-omega model exhibits higher accuracy in predicting flow field structures such as separation flowsinduced by reverse pressure gradients. It demonstrates superior capability in forecasting flow fieldcharacteristics including shock waves, pressure recovery, and airflow mixing [44, 45]. In this study, theSST k-omega turbulence model was selected for prediction, as it is widely used in airfoil flow simulation

$$\frac{\partial}{\partial t}(\rho k) + \frac{\partial}{\partial x_i}(\rho k u_i) = \frac{\partial}{\partial x_j}[\Gamma_k \frac{\partial k}{\partial x_j}] + \tilde{G}_k - Y_k \tag{5}$$

$$\frac{\partial}{\partial t}(\rho\omega) + \frac{\partial}{\partial x_i}(\rho\omega u_i) = \frac{\partial}{\partial x_j}\left[\Gamma_\omega \frac{\partial \omega}{\partial x_j}\right] + G_\omega - Y_\omega + D_\omega \tag{6}$$

where $\tilde{G}_k$ and G_ω represent the production terms of k and ω , Y_k and Y_ω represent the dissipation terms of k and ω , Γ_k and Γ_ω represent the effective diffusivity of k and ω , and finally D_ω represents the cross-diffusion term.

2.2. Deep Learning

Unlike traditional fully connected neural networks, CNNs utilize convolutional operations instead of fully connected mapping. They perform feature extraction through local receptive fields and parameter sharing while simultaneously introducing pooling to enhance translation invariance and reduce computational complexity (as shown in Figure 1). Figure 1 illustrates the CNN neural network framework. As depicted in Figure 1, a CNN comprises an input layer, hidden layers (nonlinear activation and normalization), and an output layer.

Typically, CNNs can process airfoil flow fields as pixel images input into the network. Through successive convolutions and pooling operations, features are progressively extracted, mapping low-level pixel information into high-level feature vectors. Ultimately, a fully connected layer enables regression prediction of the airfoil flow field. Compared to traditional fully connected neural network models CNNs employ strategies of local connection weight sharing and pooling, significantly simplifying the connection parameters of neurons. The feature mapping expression for its convolution operation is as follows:

$$f_{out}(N,i) = \sigma\left[\sum_{i=1}^{Cin} W(C_{out}, j) * k(N, j) + b(C_{out})\right] \tag{7}$$

Where $\sigma(\cdot)$ denotes the activation function; $k(\cdot)$ denotes the convolution kernel; * denotes the convolutionoperation; $W(\cdot)$ denotes the weights; $b(\cdot)$ denotes the bias; N denotes the batch size; C_{in} denotes thenumber of input channels, C_{out} denotes the number of output channels.

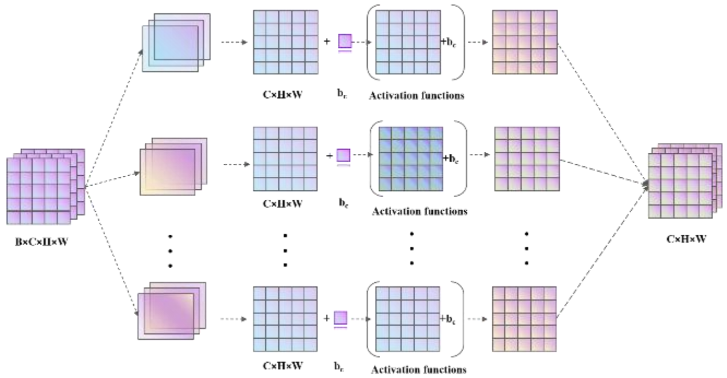

Figure 1: Schematic diagram of the CNN neural network framework

Figure 2 illustrates the U-Net neural network framework. As shown in Figure 2, compared to traditional CNNs, U-Net incorporates multi-scale feature fusion and skip-connection mechanisms, making it more suitable for point-wise prediction and reconstruction of physical quantities in flow fields. U-Net neural networks were initially developed for medical segmentation tasks in the medical field, where shallow convolutions extract low-level geometric features while deep convolutions capture high-level semantic features. U-Net employs convolutional kernels to perform feature extraction on feature maps using a sliding window approach. The formula for calculating the output feature map dimensions is as follows:

$$\begin{cases} H_{\text{out}} = \dfrac{H_{in} + 2\times P_0 - D_0 \times (K_0 - 1) - 1}{S_0} + 1 \\ W_{\text{out}} = \dfrac{W_{in} + 2\times P_1 - D_1 \times (K_1 - 1) - 1}{S_1} + 1 \end{cases} \tag{8}$$

Where P_0 denotes the padding value for the input feature's four sides, D_i represents the spacing between kernel elements, K_i indicates the conyolution kernel size, and S_i denotes the stride of the convolution kernel.

Huang et al. [46] integrated high-level semantic features and low-level geometric features across different scales through multi-scale skip connections to enhance the prediction accuracy of the U-Net model. The feature mapping calculation formula is as follows:

$$X_{De}^{i} = \begin{cases} X_{En}^{i}, i = N \\ \mathcal{H}\left(\left[\underbrace{\mathcal{C}\left(D\left(X_{En}^{k}\right)\right)_{k=1}^{i-1}, \mathcal{C}\left(X_{En}^{i}\right)}_{\text{Scales:}1^{th}\sim i^{th}}, \underbrace{\mathcal{C}\left(U\left(X_{De}^{k}\right)\right)_{k=1}^{i-1}}_{\text{Scales:}1^{th}\sim i^{th}}\right]\right), \\ i = 1, \ldots, N-1 \end{cases} \tag{9}$$

where $D(\cdot)$ and $U(\cdot)$ denotes down-sampling and denotes up-sampling, $C(\cdot)$ represents the convolution operation, and $H(\cdot)$ indicates the aggregation of multi-scale features.

Raissi et al. [47] recovered physically consistent flow field structures from limited, noisy flow visualization observations by introducing the Navier-Stokes equations in weak form into deep learning models, utilizing physical a priori constraints to constrain the data-driven inference process. This paper embeds a physical information soft-constraint loss into the training loss of the U-Net neural network model. Figure 3illustrates the Schematic diagram of physical-informed soft constraints. As shown in Figure 3, the physical-informed soft constraints component comprises residual constraints for both the continuity equation and the momentum equation. The physical information soft-constrained partial differential equation in this paper is as follows.

$$\mathcal{L}_{phy} = \lambda_{div}\mathcal{L}_{div} + \lambda_{mom}\mathcal{L}_{mom} + +\lambda_{wall}\mathcal{L}_{wall} \tag{10}$$

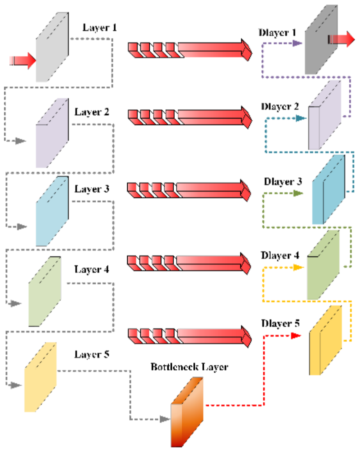

Figure 2: Schematic diagram of the U-Net neural network framework

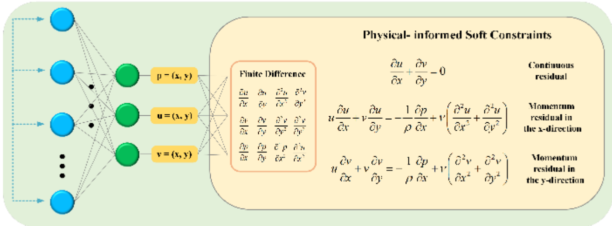

Figure 3: Schematic diagram of physical-informed soft constraints

2.3. Multi-objective optimization

Sener and Koltun [48] theoretically formalized multi-task learning as a multi-objective optimization problem and proposed a model-based goal data augmentation algorithm (MGDA) to find descent directions satisfying Pareto optimality conditions among conflicting objectives. Therefore, this paper proposes a Multi-Objective Pareto-Aware Algorithm (MOPA) for multi-objective learning. By adaptively solving the Pareto stable directions for each objective in the gradient space, it achieves collaborative optimization and balanced convergence for competing objectives. Yu et al. [49] attributed performance degradation in multi-task learning to gradient direction conflicts and proposed the Projected Conflicting Gradient Algorithm (PCGA). By projecting and correcting conflicting components at the gradient level, PCGA ensures that the joint gradient update satisfies the consistent descent condition, thereby enhancing the stability and robustness of multi-task optimization.

Therefore, to avoid the degradation of fitting accuracy caused by trade-offs in output parameters, this paper employs different multi-objective optimization algorithms during model training. Specifically, by introducing the MOPA and PCMA multi-objective optimization algorithms respectively, the competition issues arising from multiple output variables during model training are addressed, as expressed in the following equations:

$$\min_{\theta}\left(\ell_1(\theta), \ell_2(\theta), \cdots, \ell_n(\theta)\right) \tag{10}$$

where $\ell_1(\theta)$ denotes the data supervision loss, θ represents the supervision loss weighting parameter, and the objective is to find a multi-objective optimal solution within the parameter space rather than a single scalarized optimal solution.

3. Problem Statement and Results

3.1. Data setup

Figure 4 shows the comparison between measured and simulated pressure coefficients for the NACA 0012airfoil flow field. As depicted in Figure 4, the two-dimensional airfoil flow field in this study employs a structured mesh to ensure orthogonality and body-filling properties, comprising approximately 1 12,320mesh elements. The airfoil flow field employs far-field boundary conditions. To ensure numerical simulation accuracy, the height of the first layer of grid cells on the airfoil wall surface was set based on the flow operating conditions to guarantee y+ < 1.

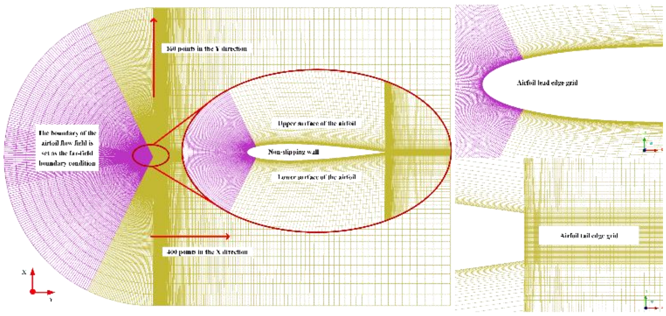

Figure 4: Grid diagram of the airfoil flow field structure of NACA0012

This study employs a density-based approach to solve the flow field around the NACA0012 airfoil. The convective term utilizes a second-order upwind scheme, while the diffusion term employs a second-order central difference scheme. Both the pressure term and viscous flux adopt central difference schemes with residuals converging to the magnitude of 1 x 10-6. The SST k-w turbulence model is employed for numerical simulation. As shown in Figure 2, the simulation results exhibit good agreement with experimental data, with pressure coefficients consistent with measured values. This indicates that the established two-dimensional airfoil flow field training database is stable and reliable.

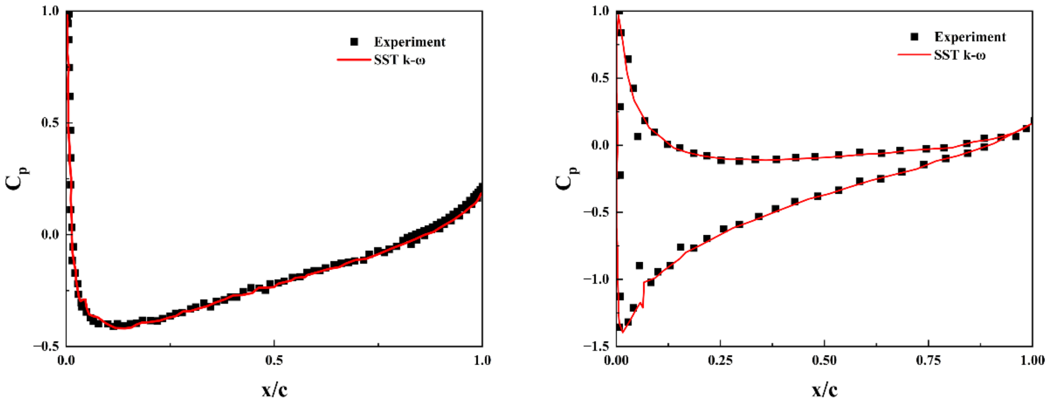

(a) Ma=0.166 AoA=0° Re=1.5×10^6 **(b) Ma=0.164 AoA=4° Re=1.5×10^6**

Figure 5: Comparison of Experimental and Simulated Pressure Coefficients for NACA0012 Airfoil

This paper employs an independently developed automated simulation software for airfoil flow simulation and aerodynamic performance analysis to establish a flow field database for the NACA0012 airfoil (as shown in Figure 3). The mesh generation and numerical simulation modules were implemented using ANSYS simulation software. The computational domain for the two-dimensional airfoil flow field includes flow conditions and fundamental flow field information. Here, denotes the angle of attack of the incoming flow to the airfoil, represents the input image coordinates, indicates the pressure in the airfoil How field, denotes the x-direction velocity in the airfoil flow field, and represents the y-direction velocity in the airfoil flow field. Based on this, the deep neural network model in this study features 6 inputs (x, y, mask, Ma, Re, AoA) and 3 outputs (p, u, v), trained using supervised learning, where mask denotes the airfoil mask. As shown in Table 1, ICEM software was employed to partition the airfoil flow field under different flow conditions, thereby establishing the two-dimensional airfoil flow field database. A random sample of 740 flow field data sets was selected, with 809 allocated for model training and 209for model testing.

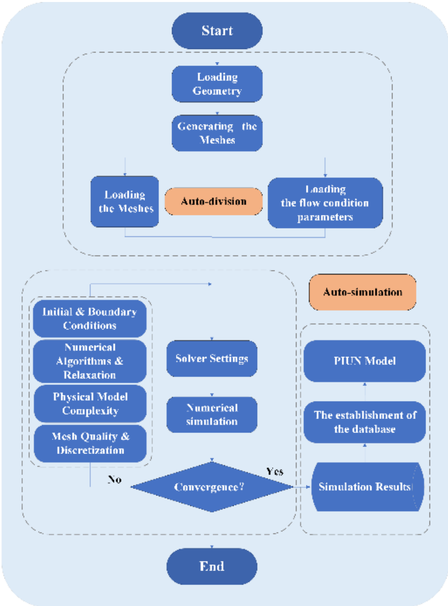

Figure 6: Flowchart of Automated Airfoil Flow Field Simulation

Table 1: Flowchart of Automated Airfoil Flow Field Simulation

Parameter	Value	Number
Mach	0.1 – 0.3	11
Reynolds	$3.0 \times 10^6 - 9.0 \times 10^6$	7
AOA	−1.0 – 8.0	10

3.2. Prediction Results

Figure 4 shows the loss function curve of the U-Net neural network across different batch sizes. To analyze the impact of hyperparameters on U-Net training, this paper conducts sensitivity analysis on key hyperparameters. U-Net models with varying batch sizes were trained, and the corresponding loss curves are depicted in Figure 12. As shown in Figure 12, the training loss function curves of U-Net models across different batch sizes all enter a rapid decline phase after 600 epoches. Comparing the loss curves reveals that as the training batch size increases, the amplitude of loss function oscillations significantly decreases, and the decline process becomes smoother. As shown in Figure 4(e), the model training MAE loss curve converges most effectively at a training batch size of 32, exhibiting the lowest training loss 6.87×10^{-6} and validation loss 7.34×10^{-6}. Therefore, the U-Net model training loss function curve converges optimally at this batch size.

This paper evaluates the accuracy of U-Net model predictions under different flow conditions using test set data not employed during training. The performance of U-Net model in predicting flow fields around the NACA0012 airfoil was randomly tested under three flow conditions: Ma=0.16, Re=5×10^{-6} and AOA=1.0°, Ma=0.18, Re=4×10^{-6} and AOA=0.0°, and Ma=0.22, Re=6×10^{-6} and AOA=4.0°. As shown in Figure 8(b), the U-Net model's predictions exhibit high agreement with RANS-calculated pressure fields, As depicted in Figure 8(c), the maximum relative error in the U-Net model's pressure held predictions across different flow conditions was consistently 0.1, indicating the model's strong global fitting capability.

To further evaluate the predictive accuracy of the U-Net model, this paper calculates the Mean Absolute Error (AE), ean Square Error (MSE), and Root Mean Square Error (RMSE) between the predicted airfoil flow field results and the simulated airfoil flow field results.

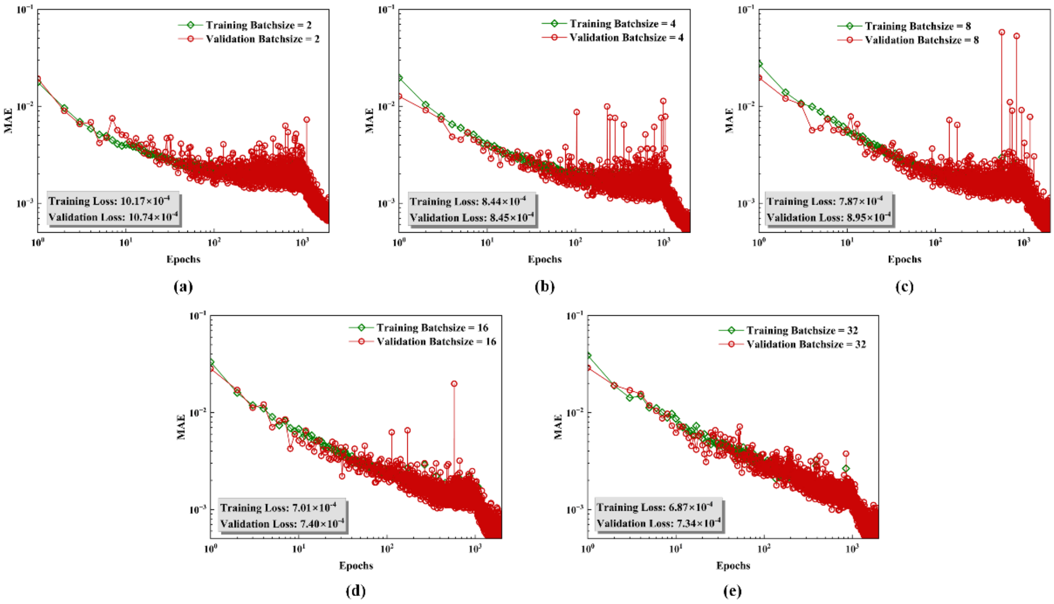

Figure 7: The curve of the loss function variation of the U-Net neural network under different batches

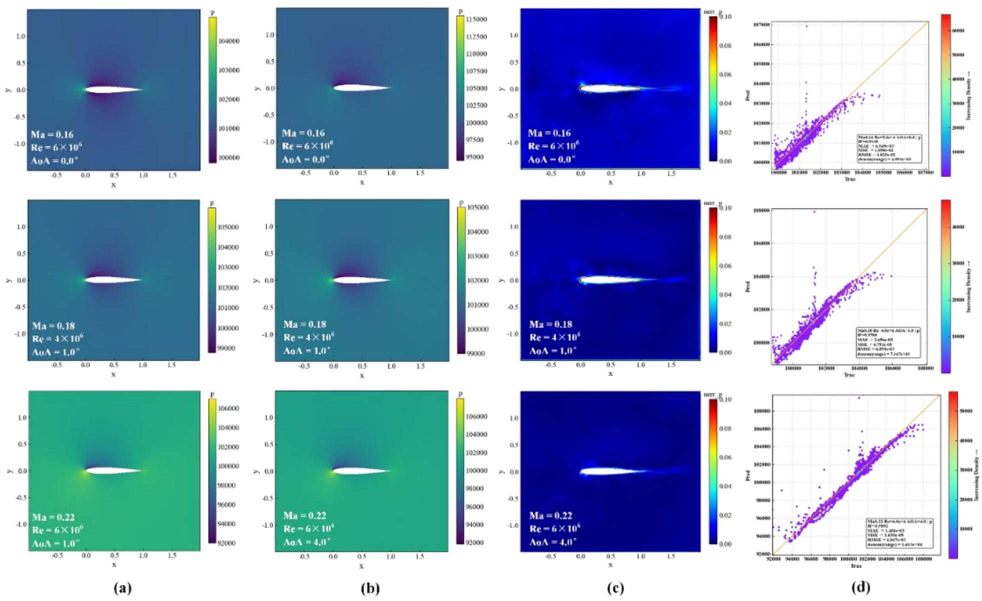

Figure 8: The curve of the loss function variation of the U-Net neural network under different batches

As shown in Figure 8(d), the scatter plot density between RANS calculation results and U-Net model predictions exhibits a diagonal distribution pattern. This indicates strong overall consistency and correlation between predicted and actual values, demonstrating the model's ability to reliably capture the general distribution characteristics of the pressure field. Furthermore, Figure 8(d) reveals that under different flow conditions, isolated points with poor correlation appear in the relative error distribution of the pressure field, predominantly concentrated in low-pressure regions.

Figure 9 shows a comparison between RANS calculation results and U-Net prediction results for the U-velocity field. As depicted in Figure 9(b), the global prediction results from the U-Net model exhibit high agreement with the RANS-calculated U-velocity field. Figure 9(c) indicates that the maximum relative error for the U-velocity field under different flow conditions is 0.1. Further analysis of the relative errors in Figure 9(c) reveals that under different flow conditions, the relative errors of the U-velocity field within the X-coordinate range of 1.5-2.0 for the airfoil flow field remain within a relatively high range of 0.02-0.06. Moreover, the relative error increases as the X-coordinate approaches the 2.0 region. This phenomenon indicates that the model's fitting accuracy in the airfoil wake region is not ideal.

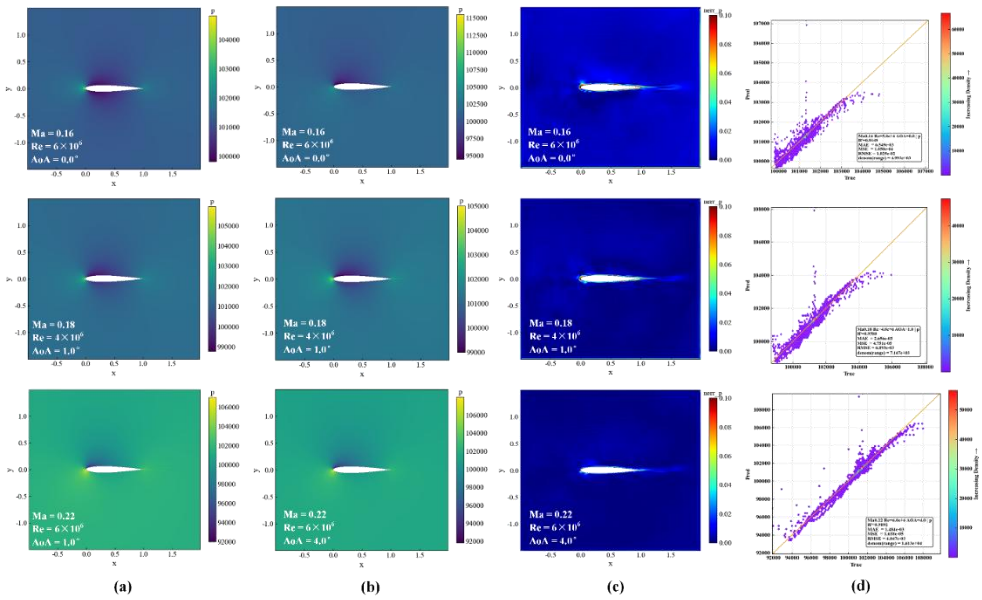

Figure 9: The curve of the loss function variation of the U-Net neural network under different batches

As shown in Figure 10, the global prediction results of the U-Net model exhibit high agreement with the V-velocity field calculated by RANS. As depicted in Figure 10(c), the maximum relative error of the -velocity field under different flow conditions is 0.1. However, the overall range of relative errors in the global prediction gradually increases with increasing angle of attack of the airfoil. Figure 10(d) reveals that the scatter plot density between RANS calculations and U-Net neural network predictions exhibits an overall diagonal distribution, indicating strong consistency and correlation between the predicted airfoil flow field and actual values. However, as shown in Figure 10(d), under flow conditions of Ma=0.22, Re=6 106 and AOA=4.0°,the predicted airfoil flow field exhibits negative correlation with actual values. This indicates a decline in the model's ability to characterize high-angle-of-attack flow states. This occurs because as the incoming flow angle increases, the external disturbance around the airfoil transitions from an attached flow to a strongly nonlinear flow state. Under the constraints of the current network architecture and loss function, the model struggles to simultaneously maintain precise depiction of the local flow structure in the high-angle-of-attack V-velocity field and effective control of the global relative error (3.0 C rectangular region). Consequently, the model predictions exhibit consistent overall distribution but an increased error range across the entire domain.

Figure 11 shows the error curves for the U velocity field in the wake region predicted by U-Net. As seen in Figures 11(c) and 11(d), the magnitude of U-velocity loss rapidly diminishes in the wake region of the airfoil, causing numerical degradation along the centerline based on extreme values. This phenomenon does not stem from insufficient model predictive capability, but rather arises because the wake region gradually transitions from a shear-dominated near-edge zone to a diffusion-dominated downstream region of the airfoil wake. During this process, the rapid decay in velocity values causes the wake region to prematurely enter a weak signal zone. Consequently, the model's relative error is amplified, and the fitting accuracy for the far-field region of the wake becomes insufficient.

Figure 12 shows a local error comparison between RANS calculation results and U-Net prediction results. As depicted in Figure 12, the relative errors in the pressure field and velocity field are most significant within the airfoil boundary layer region. Comparing the relative errors of the airfoil pressure field, U-velocity field, and V-velocity field in Figure 12 reveals that the model exhibits significantly increased relative errors in the pressure field and V-velocity field. This is because, in the momentum equation, nonlinearity primarily manifests as variations in the velocity gradient within the convective term.

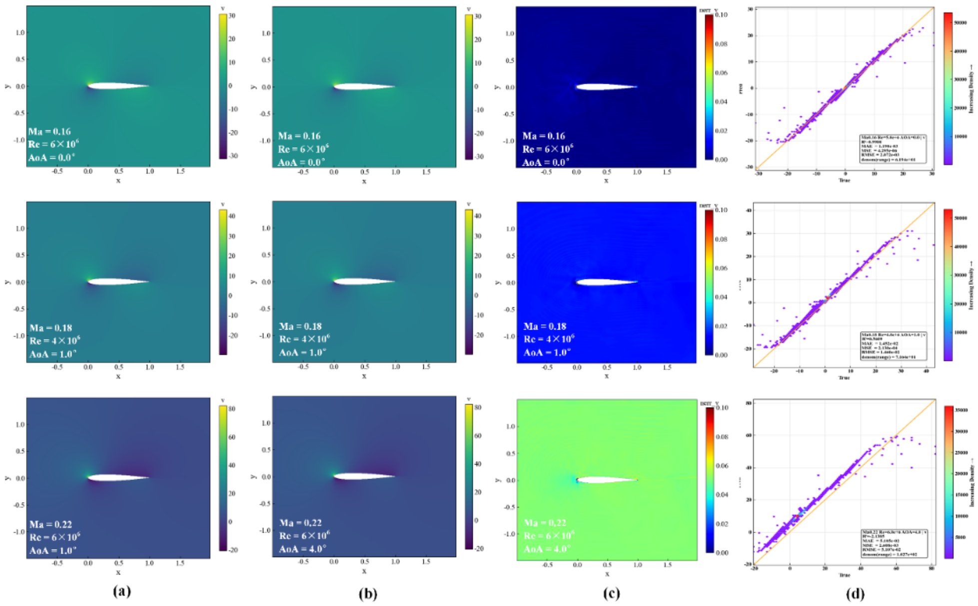

Figure 10: Comparison V-velocity field between the RANS computational results and the predicted results of the U-Net

As shown in Figure 12(a), under low Mach number, high Reynolds number, and low angle-of-attack flow conditions, the flow field around the airfoil is predominantly laminar, resulting in a thin boundary layer. Due to the high Reynolds number, the tangential velocity gradient in the normal direction significantly increases, enhancing velocity shear near the wall. This leads to the convective and shear terms dominating within the boundary layer, strengthening the coupling between pressure and velocity gradients, and thereby accentuating the nonlinear characteristics in the airfoil boundary layer region. Additionally, the curvature of streamlines sharply increases at the airfoil leading edge, causing a strong deflection of the incoming flow. This results in a significant steepening of the velocity gradient in the Y-direction near the leading edge. Consequently, the relative error in the U-velocity is primarily distributed along the boundary layer region of the airfoil, while the relative error in the V-velocity is mainly concentrated near the airfoil leading edge.

As shown in Tables 3 and 4, under flow conditions of Ma=0.16, Re=5 × 10^6 and AOA=1.0°,Ma=0.18, Re=4 × 106 and AOA=0.0°, and Ma=0.22, Re=6 × 10^6 and AOA=4.0°,the prediction errors for the pressure field and U-velocity field gradually decrease with increasing angle of attack, while the prediction error for the V-velocity field shows an increasing trend. This phenomenon indicates that the model can effectively predict the global flow field of the airfoil (as shown in Figures 5-6 and 8). This is because as the angle of attack increases, the local nonlinearity of the V-velocity field flow characteristics intensifies, making it difficult for the model to capture the local variation patterns of the V-velocity field.

As the angle of attack increases, the dominant structure of the pressure field significantly strengthens, while its small-scale perturbations and modeling errors exhibit relatively minor variations compared to the dominant structure. This results in an overall improvement in the signal-to-noise ratio of the pressure field. Notably, the prediction error of the model pressure field decreases with increasing angle of attack. This occurs because, within the current multivariate joint regression training framework, the pressure field exerts a dominant influence on the overall loss landscape due to its higher signal-to-noise ratio. Consequently, under limited model capacity, the optimization process prioritizes ensuring the prediction accuracy of the pressure field. Concurrently, the Y-direction velocity component exhibits weaker signal-to-noise ratio alongside stronger nonlinear characteristics, making its gradient direction more prone to conflicts with pressure and mainstream velocity components. Under the combined effects of limited model capacity and gradient conflicts, effective parameter updates for the Y-direction velocity are suppressed, ultimately manifesting as increased prediction errors at high angles of attack. Consequently, the MAE and RMSE of the model's pressure field prediction errors exhibit a decreasing trend at high angles of attack, while the Y-direction velocity shows the opposite pattern. This phenomenon indicates that under a unified loss function, the model struggles to achieve balanced prediction accuracy across multiple variables in a multi-physical quantity joint regression.

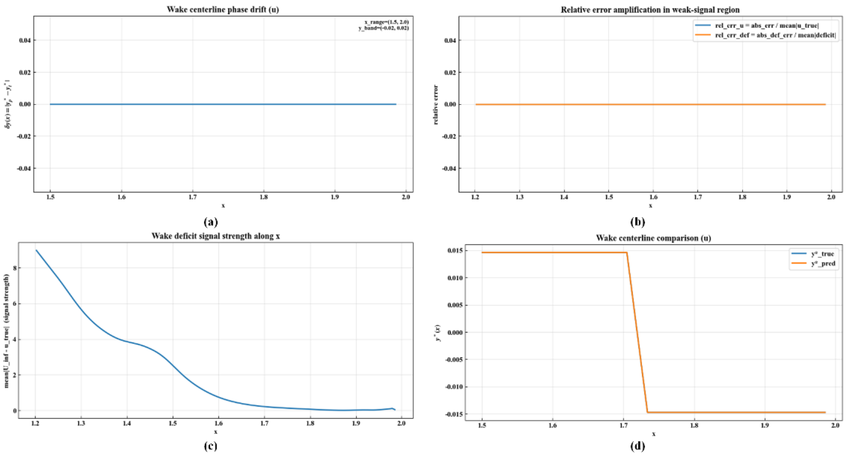

Figure 11: U-net prediction results U-velocity field wake error curve

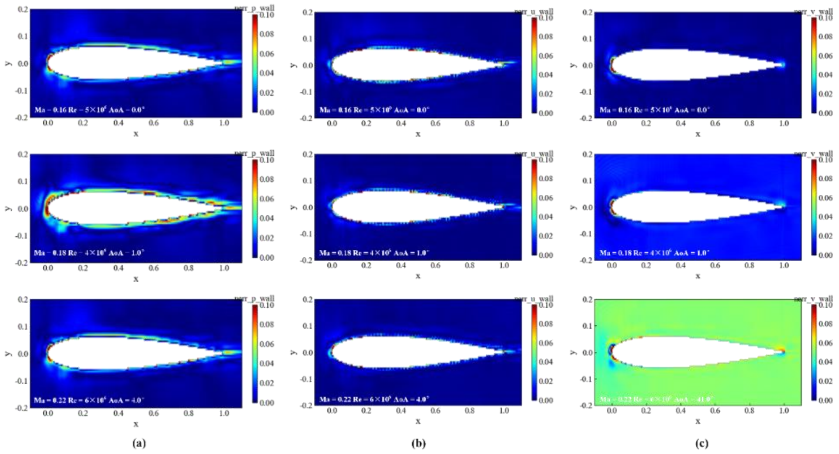

Figure 12: Comparison local error between the RANS computational results and the predicted results of the U-Net

Building upon this foundation, this paper further constructs the U-Net-Atten model and U-Net-BC model to investigate the impact of attention modules and physical constraints on model prediction accuracy. Figure 13 shows the RANS calculation results and the pressure field prediction performance of different models around the NACA0012 airfoil under flow conditions of Ma=0.16, Re=5 × 106,and AOA=0.0°. As shown in Figure 13(b), the pressure field predictions from the U-Net, U-Net-Atten, and U-Net-BC models exhibit distributions that closely match the actual values. Figure 13(c) reveals that when comparing the global relative error (3.0 C rectangular region) among U-Net, U-Net-Atten, and U-Net-BC, the U-Net-BC model exhibits the lowest global relative error (3.0 C rectangular region) among the three.

As shown in Figure 13(d), compared to the U-Net-BC model, the U-Net model exhibits the best regression performance for pressure field predictions, while the U-Net-Atten model demonstrates the worst regression performance among the three. Notably, although the U-Net-BC model exhibits the lowest global relative error (3.0 C rectangular region) and near-wall region relative error among the three models (as shown in Table 5), its prediction regression performance does not achieve a higher R^2 value than the U-Net model. This phenomenon indicates that under a unified loss function, it is challenging for a model to simultaneously balance prediction accuracy across multiple variables in multi-physical quantity joint regression.

Table 2: The MAE of U-Net model for different flow conditions

Flow condition	Pressure	Velocity U	Velocity V
Mach	6.6	1.0	1.2
Reynolds	2.7	0.6	1.5
AOA	1.5	0.2	5.1

Table 3: The RMSE of U-Net model for different flow conditions

Flow condition	Pressure	Velocity U	Velocity V
Mach	10.3	3.8	0.2
Reynolds	6.9	3.4	1.5
AOA	4.0	3.4	5.1

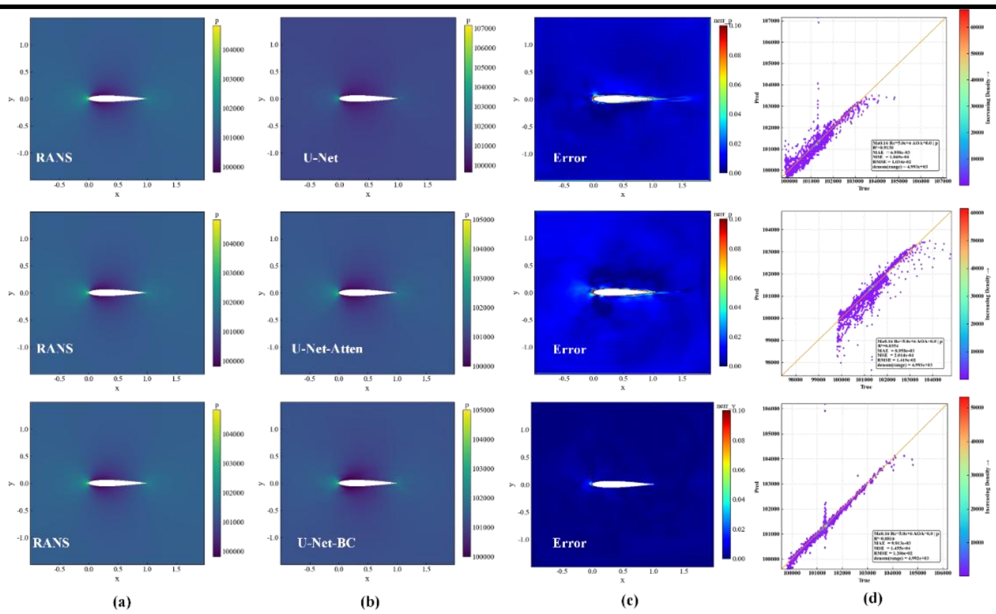

Figure 13: Comparison pressure field between the RANS computational results and the predicted results of different models

Figure 14 shows the prediction performance of the U-velocity field around the NACA0012 airfoil under flow conditions of Ma=0.16, Re=5 × 10^6 and AOA=0.0°,comparing RANS computational results with different models. As shown in Figure 14(b), the pressure field prediction distributions of the U-Net model, U-Net-Atten model, and U-Net-BC model are generally consistent with the actual values. Figure 14(c) reveals that when comparing the global relative error (3.0 C rectangular region) among the U-Net, U-Net-Atten, and U-Net-BC models, the U-Net-BC model exhibits the lowest global relative error (3.0 C rectangular region) among the three. Figure 14(d) shows that the R^2 values for the U-Net, U-Net-Atten, and U-Net-BC models are 0.98, 0.97, and 0.99, respectively. Among these, the U-Net-BC model exhibits the highest regression quality for U-velocity field predictions. This indicates that the U-Net-BC model provides the optimal fitting performance for the U-velocity field. Comparing Figures 14(c) and 14(d) and Figures 15(c) and 15(d), the U-Net-BC model demonstrates superior performance across both metrics: the global relative error (3.0 C rectangular region) and the relative error near the airfoil wall. Simultaneously, the regression fitting coefficients R^2 for the V-velocity field predictions of the U-Net, U-Net-Atten, and U-Net-BC models all exceed 0.99. Notably, the U-Net-BC model exhibits a uniformly distributed V-velocity field along the regression curve, achieving an exceptionally high R^2 of 0.998. This demonstrates that the U-Net-BC model provides the optimal fitting performance for the V-velocity field.

Table 4 presents the average relative error values for different models. As shown in Table 4, after comparing U-Net, U-Net-Atten, and U-Net-BC, the U-Net-BC model exhibits the smallest average relative error in predictions. Comparing the average relative errors between U-Net-BC and U-Net-Atten reveals that the attention mechanism does not reduce the average relative error of its predictions. Furthermore, Figures 13–15 indicate that the attention mechanism did not significantly reduce the relative errors in the pressure and velocity fields of the airfoil. This suggests that the introduction of the attention mechanism does not necessarily lead to performance improvements.

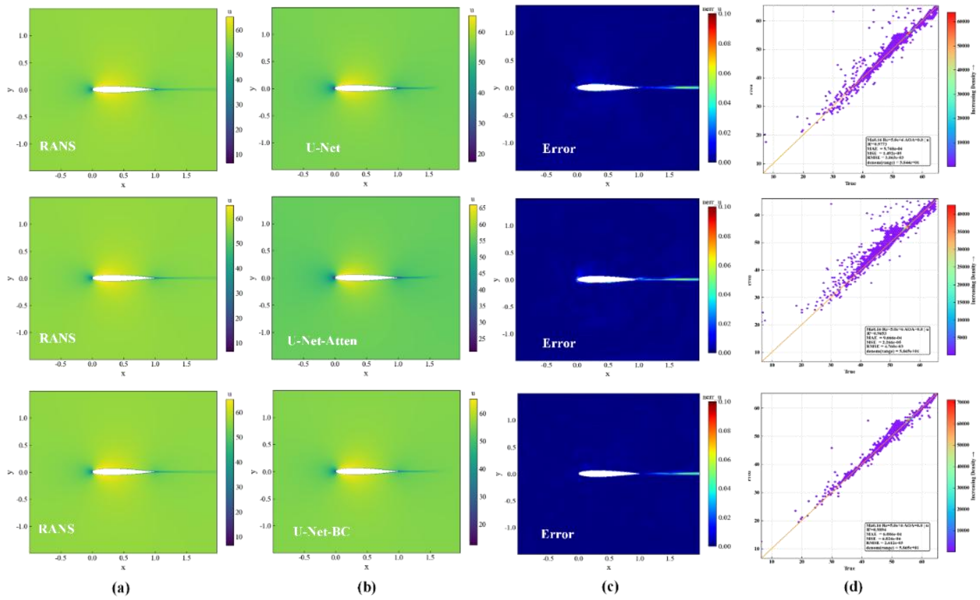

Figure 14: Comparison U velocity field between the RANS computational results and the predicted results of different models

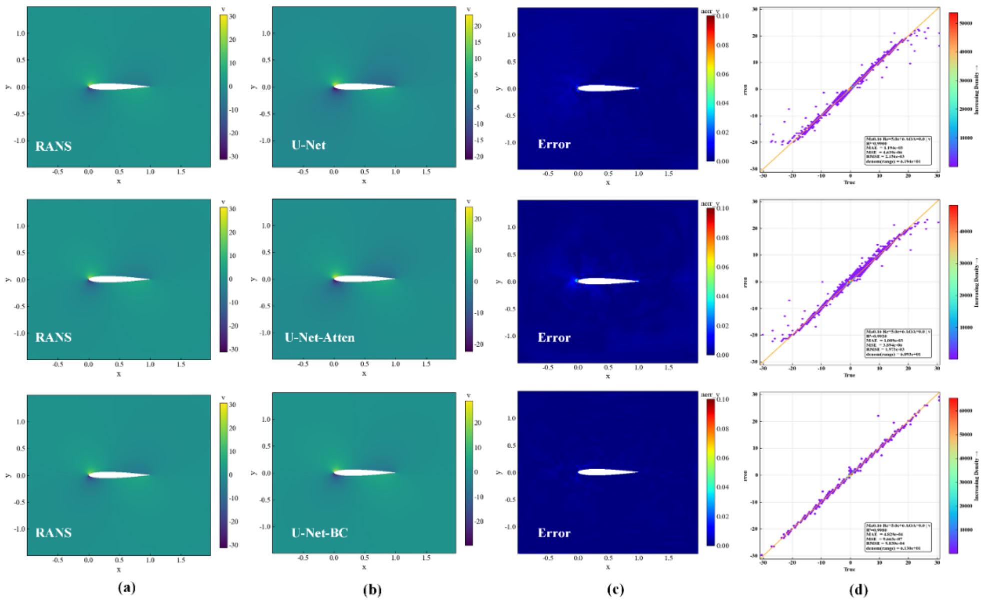

Figure 15: Comparison U velocity field between the RANS computational results and the predicted results of different models

As shown in Table 4, the U-Net-Atten model exhibits smaller global and local mean relative errors for pressure field predictions compared to the U-Net model, but larger global and local mean relative errors for velocity field predictions. Concurrently, the MAE and RMSE of U-Net predictions exhibit opposite trends. This phenomenon indicates that physical constraints effectively enhance model prediction accuracy. Simultaneously, since all neural network models were trained using single-objective optimization, improvements in prediction accuracy inevitably involve trade-offs between different objectives. Specifically, enhancing prediction accuracy for one objective typically results in reduced accuracy for others. Consequently, during training, the model experiences competing improvements between pressure and velocity fields.

In fact, the attention mechanism in this paper essentially performs data saliency reweighting rather than modeling physical significance. As shown in Figure 16, the channel attention in this paper exhibits degradation. The fundamental reason lies in the fact that airfoil flow field prediction is a spatially dominant continuous regression task. Different channels exhibit no significant differences in global statistical terms, leading to a lack of learnable discriminative directions in the channel reweighting mechanism. This ultimately converges to an approximate constant mapping. As depicted in Figure 17, spatial attention weights across different scales primarily exhibit coarse-grained responses to the overall airfoil region, failing to form continuous high-weight bands along the wall boundary layer. Simultaneously, attention tends to become blocky at deep, low-resolution features, further weakening effective focusing on the thin-layer flow structure near the wall. This misaligned reweighting not only fails to introduce new information but also distorts the original feature distribution, leading to constrained model expression and even reduced prediction accuracy. Consequently, blindly adding attention layers can degrade the original model's fitting performance rather than enhance it.

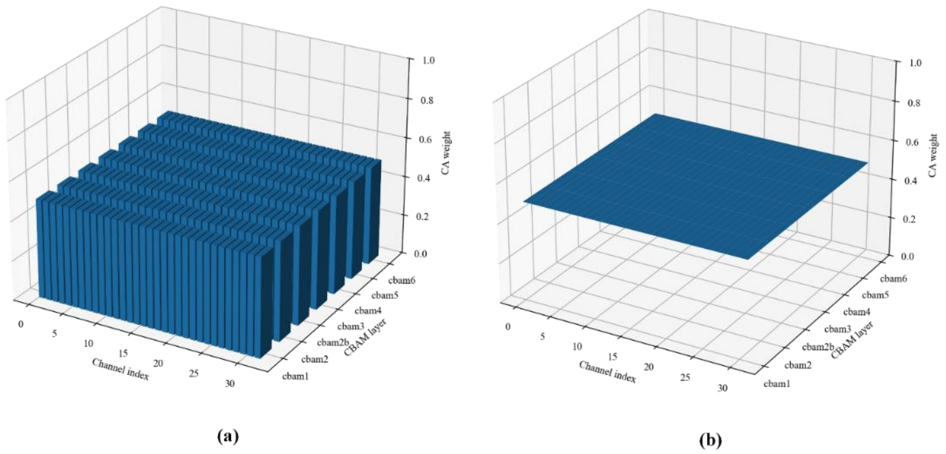

Figure 16: Channel Attention of U-Net-Atten Model

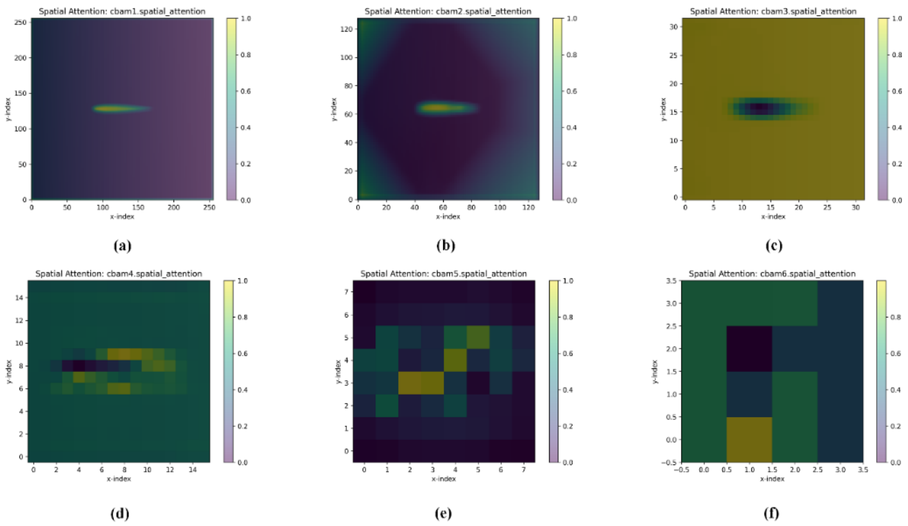

Figure 17: Spatial Attention of U-Net-Atten Model

In fact, the attention mechanism in this paper essentially performs data saliency reweighting rather than modeling physical significance. As shown in Figure 16, the channel attention in this paper exhibits degradation. The fundamental reason lies in the fact that airfoil flow field prediction is a spatially dominant continuous regression task. Different channels exhibit no significant differences in global statistical terms, leading to a lack of learnable discriminative directions in the channel reweighting

mechanism. This ultimately converges to an approximate constant mapping. As depicted in Figure 17, spatial attention weights across different scales primarily exhibit coarse-grained responses to the overall airfoil region, failing to form continuous high-weight bands along the wall boundary layer. Simultaneously, attention tends to become blocky at deep, low-resolution features, further weakening effective focusing on the thin-layer flow structure near the wall. This misaligned reweighting not only fails to introduce new information but also distorts the original feature distribution, leading to constrained model expression and even reduced prediction accuracy. Consequently, blindly adding attention layers can degrade the original model's fitting performance rather than enhance it.

Furthermore, based on the U-Net neural network framework, this paper successively establishes the U-MO-P model and U-MO-G model to investigate the impact of multi-objective optimization strategies on model prediction accuracy. As shown in Figure 18, the pressure field prediction results of U-Net and U-MO-P exhibit generally correct trends, but both models show some dispersion of data points in high-pressure regions. U-MO-G demonstrates the best curve-fitting performance for its data points, which are also the most concentrated, with significantly reduced dispersion in high-pressure zones. This phenomenon indicates that U-MO-G demonstrates significant advantages in pressure field prediction, particularly in high-pressure gradient regions, where its gradient conflict resolution mechanism is more conducive to maintaining consistent optimization of the pressure-velocity field.

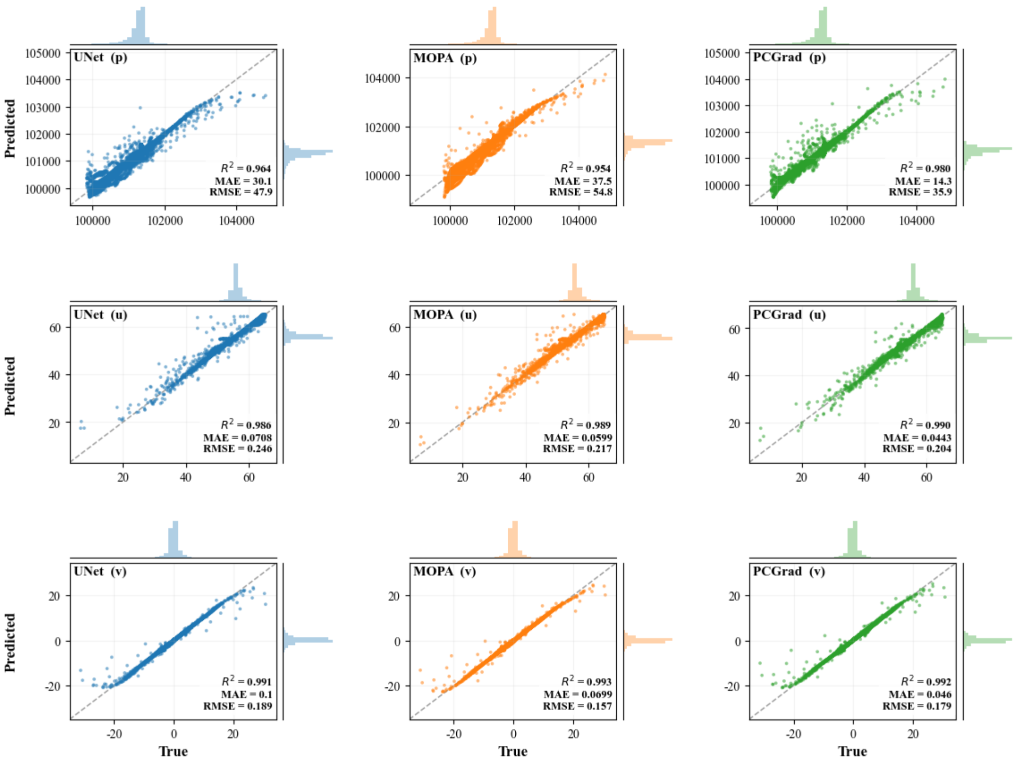

Figure 18: Regression graph of RANS calculation results versus prediction results of different models

Furthermore, the three models exhibit consistent predictions for the U-velocity field, indicating that for variables dominated by mainstream velocity, the model structure itself possesses sufficient expressive capability, with multi-objective optimization methods yielding only marginal improvements. Compared to the V-velocity field predictions of U-Net and U-MO-P, U-MO-G achieves the lowest R^2 and MAE values. Compared to the V-velocity field predictions of U-Net and U-MO-G, U-MO-P exhibits the smallest RMAE value. This phenomenon indicates that U-MO-G achieves relatively higher overall and local fitting accuracy, while U-MO-P tends toward global error balancing, which is related to the algorithm's inherent optimization capabilities.

Figure 19 shows the average relative error of different model predictions under flow conditions of Ma=0.16, Re=5 × 10^6,and AOA=1.0°.As depicted in Figure 19, the U-MO-G model achieves the lowest error in both pressure field and velocity field predictions, demonstrating a particularly significant advantage in normal velocity. This phenomenon indicates that the gradient conflict resolution algorithm exhibits lower average errors and more concentrated distribution characteristics in predicting pressure extreme regions and the y-direction velocity component. This demonstrates that its gradient conflict resolution mechanism possesses superior stability and robustness during multi-objective optimization. Furthermore, the difficulty in reducing local errors stems from the highly nonlinear nature of model parameter updates in pressure extreme regions and the y-direction velocity component. Traditional multi-objective optimization methods based on loss space trade-offs struggle to avoid sacrificing local regions.

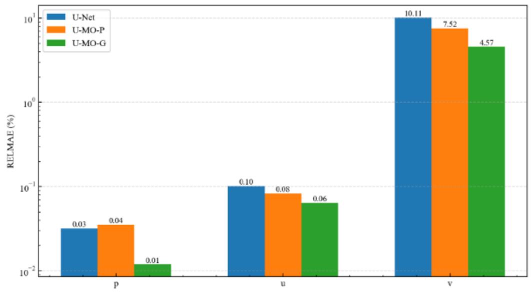

Figure 19: Average relative error of prediction results from different models under the Ma=0.16 Re=5×10^6 AOA=1.0° flow conditions

Table 4: Average relative errors of different models

Physical Quantity	Average Relative error	U-Net(%)	U-MO-P(%)	U-MO-G(%)
Pressure	Global	1.13	1.53	0.79
	Local	6.29	6.16	4.82
Velocity	Global	0.13	0.14	0.13
	Local	2.47	2.34	2.31

As shown in Table 5, The average global relative error (3.0 C rectangular region) and average local relative error (0.02 C rectangular region) of the U-MO-G predicted pressure field were both significantly reduced compared to U-Net. The former showed a 30% reduction in average global relative error (3.0 C rectangular region) and a 21.7% reduction in average local relative error (0.02 C rectangular region) relative to the latter. Meanwhile, the average global relative error of the U-MO-G predicted velocity field (3.0 C rectangular region) was comparable to that of U-Net, while the average local relative error of the U-MO-G predicted velocity field (0.02 C rectangular region) was slightly lower than that of U-Net. This indicates that while the gradient conflict resolution mechanism further enhances the model's prediction accuracy, its fitting capability in regions with strong nonlinearity remains limited, and it still cannot significantly improve prediction accuracy in the near-wall region of the airfoil.

This paper builds upon the U-MO-G model by incorporating additional physical constraints and constructing a multi-output PIUN neural network model. Under the premise that output terms remain mutually independent, it further investigates the impact of physical constraints on the performance of the PIUN model. As shown in Figure 20, comparing the global relative error (3.0 C rectangular region) images under flow conditions of Ma=0.16, Re=5 × 106 and AOA=0.0°, Ma=0.18, Re=4 × 106 and AOA=1.0°, and Ma=0.22, Re=6 × 10^6 and AOA=4.0°,it is evident that the local relative error (0.02 C rectangular region) of PIUN predictions generally increases compared to the global relative error (3.0 C rectangular region) of U-Net predictions. The global relative errors (3.0 C rectangular region) for the pressure field and velocity field increase by 58.4% and 23.1%, respectively (as shown in Table 9).

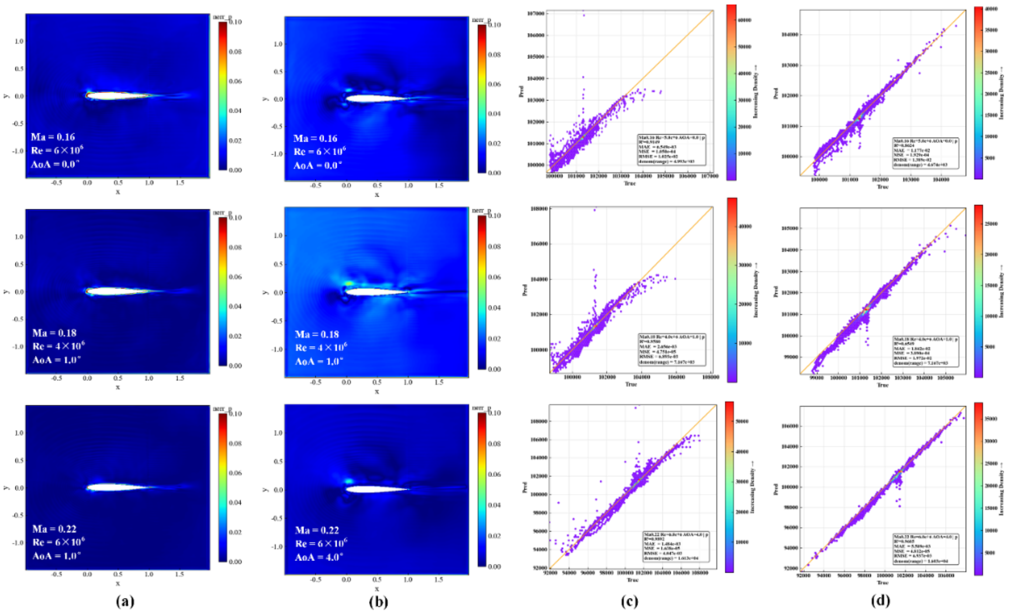

Figure 20: Comparison chart of global error between U-Net and PIUN pressure field prediction results

As shown in Figure 21, comparing the flow conditions of Ma=0.16, Re=5 × 10^6 and AOA=0.0°, Ma=0.18, Re=4 × 10^6 and AOA=1.0°,and Ma=0.22, Re=6 × 10^6 and AOA=4.0°,the local relative error (0.02 C rectangular region) of the PIUN prediction results decreased. This phenomenon indicates that physical constraints can enhance the prediction accuracy of the pressure field near the wall surface in the flow region, but the global relative error (3.0 C rectangular region) increases. This is because physical constraints tend to suppress local extrema and high-gradient structures, amplifying errors in high-gradient, strongly nonlinear regions and dominating the global statistics. Consequently, the global relative error (3.0 C rectangular region) of the pressure field increases.

Figure 22 shows the comparison of global relative errors (3.0 C rectangular region) under flow conditions of Ma=0.16, Re=5 × 10^6 and AOA=0.0°,Ma=0.18, Re=4 × 10^6 and AOA=1.0°, and Ma=0.22, Re=6 × 106 and AOA=4.0°,the relative error in the wake region of the PIUN prediction shows a slight reduction. As shown in Figure 23, comparing the local relative error (0.02 C rectangular region) images under flow conditions of Ma=0.16, Re=5 × 106 and AOA=0.0°,Ma=0.18, Re=4 × 10^6 and AOA=1.0°,and Ma=0.22, Re=6 × 10^6 and AOA=4.0°,the local relative error (0.02 C rectangular region) images reveal that the local relative error (0.02C rectangular region) of the PIUN prediction results has decreased. This phenomenon indicates that physical constraints enhance the prediction accuracy of the U-velocity field near the wall in the flow region, while multi-head outputs indirectly correct relative errors in the wake region. The latter correction arises from the downstream structural consistency induced by wall physical constraints through continuity. The multi-head design ensures this correction does not compromise the freedom of expression in the wake.

Figure 24 shows the local relative error (0.02 C rectangular region) images comparing predictions under flow conditions of Ma=0.16, Re=5 × 10^6 and AOA=0.0°, Ma=0.18, Re=4 × 10^6 and AOA=1.0°,and Ma=0.22, Re=6 × 10^6 and AOA=4.0°,the relative global error between PIUN and U-Net predictions shows no significant difference. However, the relative error of the V-velocity field predicted by PIUN in the leading edge region of the airfoil is significantly smaller than that of the V-velocity field predicted by U-Net. This phenomenon indicates that physical constraints can enhance the prediction accuracy of the V-velocity field near the wall surface of the airfoil.

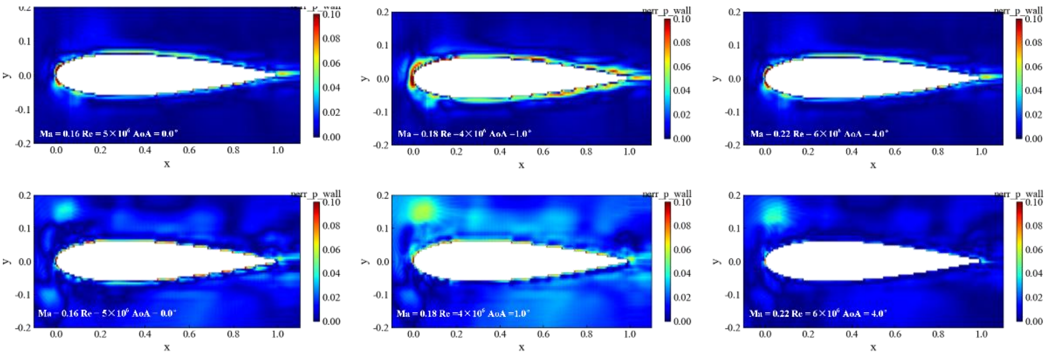

(a) (b) (c)

Figure 21: Comparison chart of local errors between U-Net and PIUN pressure field prediction results

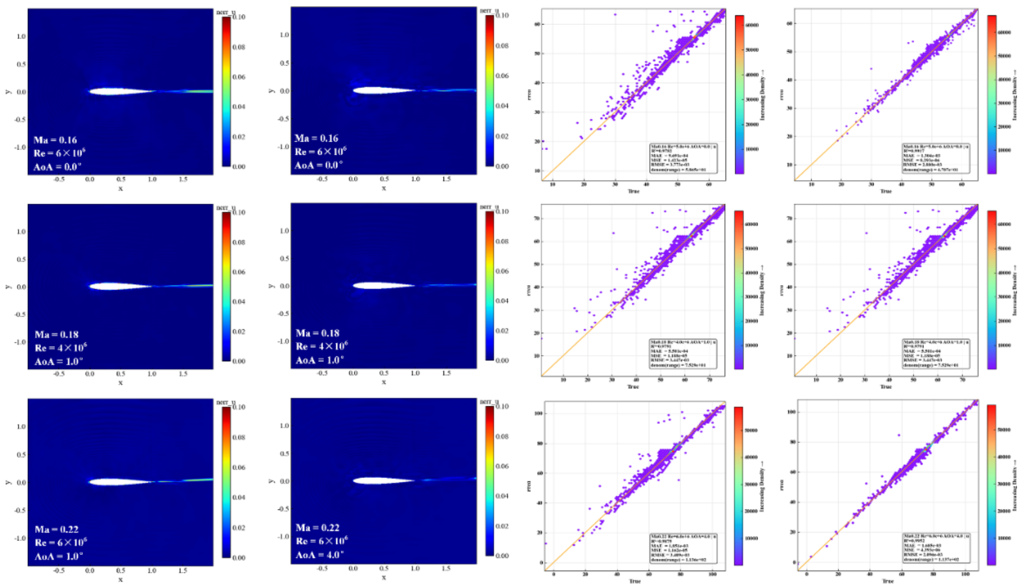

(a) (b) (c) (d)

Figure 22: Comparison chart of local errors between U-Net and PIUN pressure field prediction results

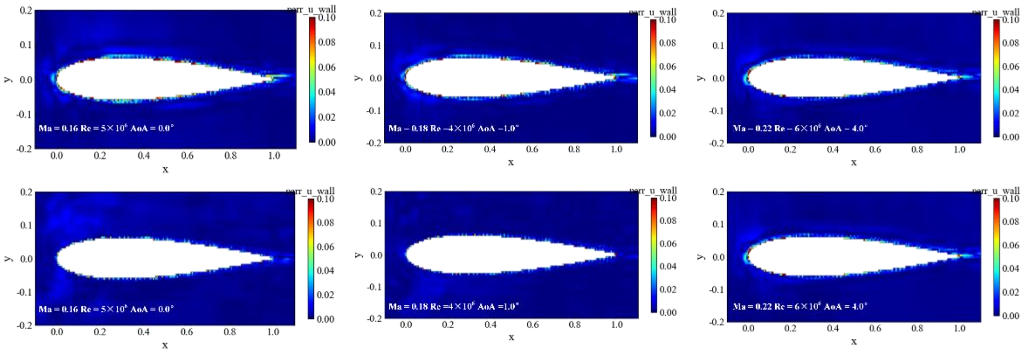

(a) (b) (c)

Figure 23: Comparison chart of local errors between U-Net and PIUN pressure field prediction results

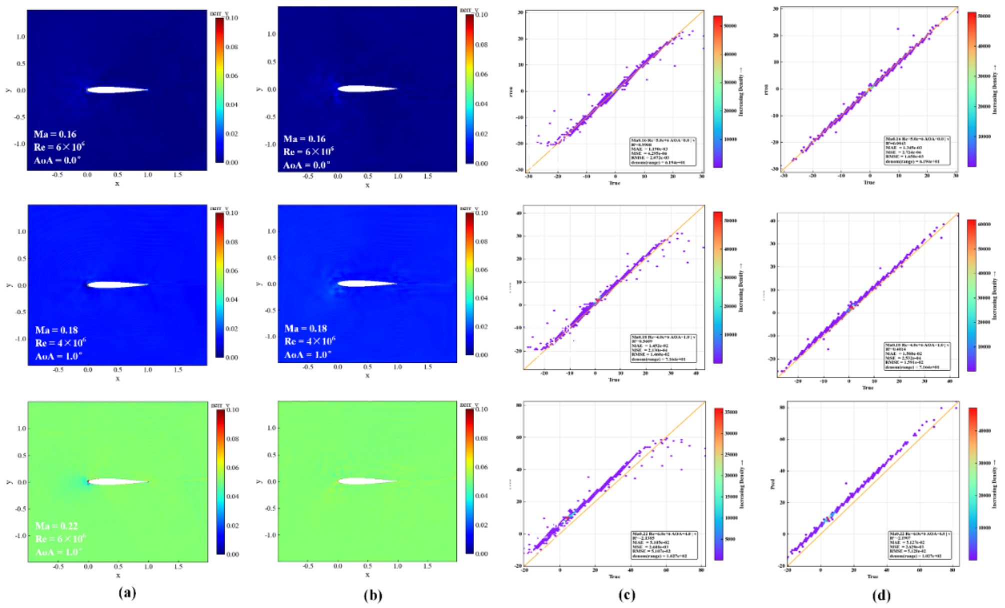

Figure 24: Comparison chart of global error between U-Net and PIUN pressure field prediction results

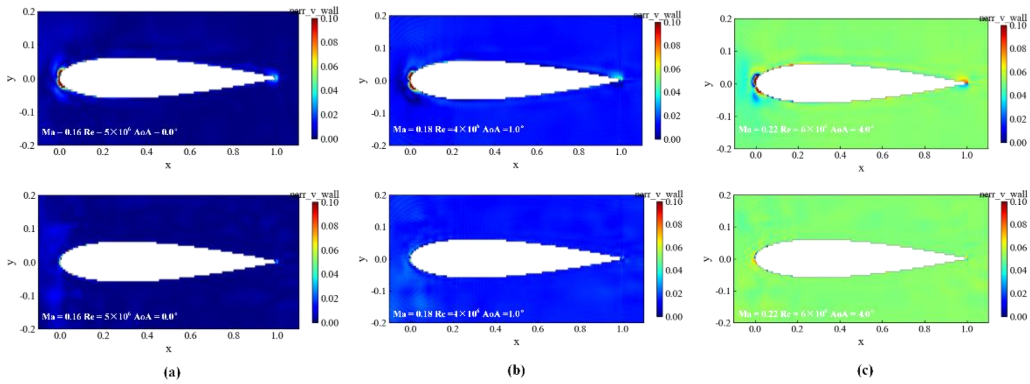

Figure 25: Comparison chart of local errors between U-Net and PIUN pressure field prediction results

As shown in Table 7, under flow conditions of Ma=0.16, Re=5 × 10^6 and AOA=0.0°,Ma=0.18, Re=4 × 10^6 and AOA=1.0°, and Ma=0.22, Re=6 × 10^6 and AOA=4.0°, the PIUN prediction shows a slight improvement in global relative error (3.0 C rectangular region) compared to the U-Net prediction, but a significant decrease in local relative error (0.02 C rectangular region). This indicates that enhancing prediction accuracy in the near-wall region of the airfoil flow field through physical constraints comes at the cost of reduced global fitting accuracy. Tables 8–9 reveal that for Ma=0.16, Re=5 × 106 and AOA=0.0°, Ma=0.18, Re=4 × 106 and AOA=1.0°,and Ma=0.22, Re=6 × 106 and AOA=4.0°, the overall trend of prediction errors between PIUN and U-Net is consistent, with no significant reduction observed in the former. Under high-angle-of-attack flow conditions, the PIUN model demonstrates significantly improved prediction accuracy for the pressure field and U-velocity field, while the error in the V-velocity field relatively increases. This stems from the V-velocity's physically smaller magnitude, stronger local gradients, and more complex geometric-pressure coupling characteristics, making it more prone to conflicts with both pressure and V-velocity gradient directions during multi-objective optimization. Simultaneously, this indicates that while the PCGrad algorithm mitigates gradient conflicts between multi-physical quantities during training, it remains challenging to fully eliminate the mutual influence among multi-physical outputs caused by large gradients and strong nonlinearities.

Table 5: Average relative errors of different models

Physical Quantity	Average Relative error	U-Net	PIUN
Pressure	Global	1.13	1.79

	Local	6.29	2.44
Velocity	Global	0.13	0.16
	Local	2.47	1.02

Table 6: The MAE of U-Net model for different flow conditions

	Flow condition	Pressure	Velocity U	Velocity V
U-Net	Condition 1	6.6	9.7	1.2
	Condition 2	2.7	5.5	1.5
	Condition 3	1.5	1.9	5.1
PIUN	Condition 1	11.8	13.0	1.4
	Condition 2	18.4	5.5	1.6
	Condition 3	5.6	1.7	5.1

Table 7: The RMSE of U-Net model for different flow condition

	Flow condition	Pressure	Velocity U	Velocity V
U-Net	Condition 1	10.3	9.7	1.2
	Condition 2	6.9	5.5	1.5
	Condition 3	4.0	1.9	5.1
PIUN	Condition 1	13.9	2.88	0.17
	Condition 2	19.7	3.45	1.59
	Condition 3	6.94	2.10	5.13

4. Conclusion and Future Work

This paper addresses the rapid prediction of two-dimensional airfoil flow fields by designing six model variants. Under unified data partitioning and training budgets, we compared baseline U-Net, generic attention modules, and weak physical constraints. Current findings indicate:

For regular grid airfoil flow prediction, the U-Net model demonstrates strong global fitting capabilities, enabling rapid two-dimensional airfoil flow prediction. Forcing the attention mechanism does not necessarily reduce prediction errors in pressure and velocity fields. Comparative test results show that on the test set, the U-Nat-Atten model achieves a maximum improvement of 77% in global relative error (3.0 C rectangular region) and 30% in local relative error (0.02 C rectangular region) compared to U-Net. The introduction of physical constraints effectively reduces prediction errors in both pressure and velocity fields. Comparative test results indicate that on the test set, the U-Nat-BC model achieves a maximum reduction of 20% in global relative error (3.0 C rectangular region) and 74% in local relative error (0.02 C rectangular region) compared to U-Net. Predicting multi-physics fields in two-dimensional airfoil flow essentially involves a multi-objective optimization problem. During joint training of multiple physical quantities, conflicting objectives arise, limiting a single model's ability to simultaneously minimize prediction errors across all physical quantities under different operating conditions.

Introducing physical constraints significantly improves physical consistency metrics such as boundary condition satisfaction and equation residuals. However, this improvement does not directly translate into a synchronous reduction in global regression error. This primarily stems from potential directional inconsistencies between the data-fitting objective and the physical residual objective in the gradient space, leading to objective competition during optimization updates and hindering synchronous error reduction. Comparative test results demonstrate that on the test set, the PIUN model achieves a maximum reduction of 61.2% in local relative error (0.02 C rectangular region) compared to U-Net; while the global relative error (3.0 C rectangular region) increased by up to 58.4% compared to U-Net.

Subsequent work will be developed based on the prior processing of airfoil geometry, aligning feature reweighting with the physical structure of critical flow regions to enhance the expressive capability and prediction stability of the existing U-Net framework under highly nonlinear operating conditions.

Acknowledgements

This study was funded by the National Natural Science Foundation of China (Grant No. 52201356).

References

[1] Slotnick J. K. Cfd vision 2030 study: A path to revolutionary computational aero-sciences. Technical report, NASA, 2014.

[2] Elimelech Y., Arieli R., and Iosilevskii G. Flow over naca-0009 and eppler-61 airfoils at Reynolds numbers 5000 to 60,000. AIAA Journal, 45(10), 2007.

[3] Lyu Z., Kenway G. K. W., and Martins J. R. R. A. Aerodynamic shape optimization investigations of the common research model wing benchmark. AIAA Journal, 53(4): 968–985, 2015.

[4] LeDoux S. T., Vassberg J. C., Young D. P., Fugal S., Kamenetskiy D., Huffman W. P., Melvin R. G., and Smith M. F. Study based on the aiaa aerodynamic design optimization discussion group test cases. AIAA Journal, 53: 1910–1935, 1935.

[5] Kenway G. K. W. and Martins J. R. R. A. Multipoint aerodynamic shape optimization investigations of the common research model wing. AIAA Journal, 54(1): 113–128, 2016.

[6] Anderson W. K., Ahrabi B. R., and Newman J. C. Finite element solutions for turbulent flow over the naca 0012 airfoil. AIAA Journal, 54(9), 2016.

[7] Sato M., Asada K., Nonomura T., Kawai S., and Fujii K. Large-eddy simulation of naca 0015 airfoil flow at reynolds number of 1.6 × 10^6. AIAA Journal, 55(2), 20175.

[8] Hrynuk J. T., Olson D., Stutz C., and Jackson J. Effects of turbulence on naca 0012 airfoil performance at low reynolds number. AIAA Journal, 62(1), 2024.

[9] Sekar V., Jiang Q., Shu C., and Khoo B. C. Fast flow field prediction over airfoils using deep learning approach. Physics of Fluids, 31(5), 2019.

[10] Zhang Y., Wang T., and Zhang X. Motrv2: Bootstrapping end-to-end multi-object tracking by pretrained object detectors. Proceedings of the IEEE/CVF Conference on Computer Vision and Pattern Recognition, 22056–22065, 2065.

[11] Tinn R., Cheng H., Gu Y., et al. Fine-tuning large neural language models for biomedical natural language processing. Patterns, 4(4): 100729, 2023.

[12] Chitta K., Prakash A., Jaeger B., et al. TransFuser: Imitation with Transformer-Based Sensor Fusion for Autonomous Driving. IEEE Transactions on Pattern Analysis and Machine Intelligence, 45(11): 12878–12895, 2023.

[13] Li J., Du X., and Martins J. R. R. A. Machine learning in aerodynamic shape optimization. Progress in Aerospace Sciences, 134(1), 2022.

[14] Kou J. and Zhang W. Data-driven modeling for unsteady aerodynamics and aeroelasticity. Progress in Aerospace Sciences, 2021.

[15] Wang H., Cao Y., Huang Z., et al. Recent advances on machine learning for computational fluid dynamics: A survey. Arxiv, 2023.

[16] Wang Y., Han R., Liu Z., Zhang Y., and Chen G. Progress of deep learning modeling technology for fluid mechanics. Acta Aeronautica et Astronautica Sinica, 524779–524779, 2021.

[17] Shu, Q., Jin Q., Gao C., et al. The new paradigm of comsputational fluid dynamics: Empowering computational fluid dynamics with machine learning. Physics of Fluids, 2025.

[18] Sun D., Wang Z., Qu F., and Bai J. A Deep Learning Based Prediction Approach For The Supercritical Airfoil at Transonic Speeds. Physics of Fluids, 2021.

[19] Thuerey N., Weißenow K., Prantl L., et al. Deep learning methods for Reynolds-averaged Navier–Stokes simulations of airfoil flows. AIAA Journal, 58(1): 25–36, 2020.

[20] Chen J., Viquerat J., and Hachem E. U-net architectures for fast prediction of incompressible laminar flows. arXiv:1910.13532, 2019.

[21] Chen L. W. and Thuerey N. Towards high-accuracy deep learning inference of compressible flows over aerofoils. Computers & Fluids, 250: 105707, 2023.

[22] Brunton S. L., Noack B. R., and Koumoutsakos P. Machine learning for fluid mechanics. Annual Review of Fluid Mechanics, 134: 477–508, 2020.

[23] Duru C. Duru, 236, 2022.

[24] Sun X., Cai S., Yang Y., Lin G., and Karniadakis G. E. A comprehensive survey of physics-informed neural networks. Computer Methods in Applied Mechanics and Engineering, 378(113709), 2021.

[25] Dong S. and Ni N. A method for representing periodic functions and enforcing exactly periodic boundary conditions with deep neural networks. Journal of Computational Physics, 2021.

[26] Wang S., Teng Y., and Perdikaris P. Understanding and mitigating gradient flow pathologies in physics-informed neural networks. Journal of Computational Physics, 2021.

[27] Raissi M., Perdikaris P., and Karniadakis G. E. Physics-informed neural networks: A deep learning framework for solving forward and inverse problems involving nonlinear partial differential equations. Journal of Computational Physics, 378: 686–707, 2019.

[28] Wang S., Yu X., and Perdikaris P. On the convergence and gradient flow structures of physics-informed neural networks. SIAM Review, 2021.

[29] Karniadakis G. E. and Kevrekidis I. G. Kevrekidis, 2021.

[30] Cai S., Mao Z., Wang Z., Yin E., and Karniadakis G. E. Physics-informed neural networks (PINN) for fluid mechanics: A review. Acta Mechanica Sinica, 2021.

[31] Gao H., Sun L., and Wang J.-X. Super-resolution and denoising of fluid flow using physics-informed convolutional neural networks without high-resolution labels. Physics of Fluids, 33(7): 073603, 2021.

[32] Krishnapriyan A. S., Gholami A., Zhe S., et al. Characterizing possible failure modes in physics-informed neural networks. arXiv:2109.01050, 2021.

[33] Bischof R. and Kraus M. A. Multi-objective loss balancing for physics-informed deep learning. Computer Methods in Applied Mechanics and Engineering, 2025.

[34] Heldmann S., Herzog R., Sachs E. Biobjective optimization for physics-informed neural networks. Journal of Computational Physics, 2023.

[35] Cao Y. and Zhang Z. Alleviating ill-conditioning in physics-informed neural networks. Journal of Computational Physics, 2025.

[36] Sun L., Gao H., Pan S., and Wang J. Physics-informed neural network based on a new adaptive gradient descent algorithm for solving partial differential equations of flow problems. Physics of Fluids, 2020.

[37] Wang S., Teng Y., and Perdikaris P. Understanding and mitigating gradient flow pathologies in physics-informed neural networks. SIAM Journal on Scientific Computing, 2021.

[38] Wu C., Zhu Y., Chen Z., and Karniadakis G. E. A comprehensive study of adaptive sampling methods for physics-informed neural networks. Computer Methods in Applied Mechanics and Engineering, 2023.

[39] Bonnans J. F. and Martinon P. Second-order KKT optimality conditions for multi-objective optimal control problems. SIAM Journal on Control and Optimization, 1908–1938, 1938.

[40] Eichfelder G. Scalarization methods in multiobjective optimization. Optimization Methods and Software, 601–627, 2021.

[41] Wang S., Yu X., and Perdikaris P. FP64 is all you need: Rethinking failure modes in physics-informed neural networks. Journal of Computational Physics, 2024.

[42] Zeng Y., Wang S., and Perdikaris P. Bias–variance trade-off in physics-informed neural networks with randomized smoothing for highdimensional PDEs. SIAM Journal on Scientific Computing, A89–A118, 2024.

[43] Estep D., Larson M. G., and Williams R. D. Estimating the error of numerical solutions of systems of reaction–diffusion equations. IMA Journal of Numerical Analysis, 83–116, 2024.

[44] Zou Z., Meng X., and Karniadakis G. E. Correcting model misspecification in physics-informed neural networks. Journal of Computational Physics, 2024.

[45] Bartosiewicz Y., Aidoun Z., Desevaux P., and Mercadier Y. Numerical and experimental investigations on supersonic ejectors. International Journal of Heat and Fluid Flow, 56–70, 2005.

[46] Huang H., Lin L., Tong R., Hu H., Zhang Q., Iwamoto Y., Han X., Chen Y.-W., and Wu J. Unet 3+: A full-scale connected unet for medical image segmentation. ICASSP 2020-2020 IEEE International Conference on Acoustics, Speech and Signal Processing (ICASSP), IEEE, 1055–1059, 2020.

[47] Raissi M., Yazdani A., and Karniadakis G. E. Hidden fluid mechanics: Learning velocity and pressure fields from flow visualizations. Science, 2020.

[48] Sener O. and Koltun V. Multi-task learning as multi-objective optimization. Advances in Neural Information Processing Systems, 2018.

[49] Yu T., Kumar S., Gupta A., Levine S., Hausman K., and Finn C. Gradient surgery for multi-task learning. 34th Conference on Neural Information Processing Systems (NeurIPS 2020), Vancouver, Canada, 2020.